Journal of Molecular Catalysis A: Chemical 410 (2015) 184–192

Contents lists available at ScienceDirect

Journal of Molecular Catalysis A: Chemical

journal homepage: www.elsevier.com/locate/molcata

Catalytic decomposition of phenethyl phenyl ether to aromatics over Pd–Fe bimetallic catalysts supported on ordered mesoporous carbon

Jeong Kwon Kim, Jong Kwon Lee, Ki Hyuk Kang, Jong Won Lee, In Kyu Song*

School of Chemical and Biological Engineering, Institute of Chemical Processes, Seoul National University, Shinlim-dong, Kwanak-ku, Seoul 151-744, South Korea

ARTICLE INFO

Article history:
Received 11 August 2015
Received in revised form
17 September 2015
Accepted 27 September 2015

Keywords:
Lignin
Bimetallic catalyst
Phenethyl phenyl ether
Pd–Fe catalyst
Aromatics

ABSTRACT

A series of bimetallic Pd–Fe catalysts supported on ordered mesoporous carbon (denoted as Pd_1–Fe_X/OMC) were prepared with a variation Fe/Pd molar ratio (X), and they were applied to the catalytic decomposition of phenethyl phenyl ether to aromatics. Phenethyl phenyl ether was used as a lignin model compound for representing β-O-4 linkage in lignin. The effect of Fe/Pd molar ratio on the catalytic activities and physicochemical properties of bimetallic Pd_1–Fe_X/OMC catalysts was investigated. It was found that crystalline phase, reducibility, chemical state, and electronic property of Pd_1–Fe_X/OMC catalysts were strongly influenced by Fe/Pd molar ratio. In particular, modified electronic property derived from the interaction between Pd and Fe significantly changed the hydrogen adsorption ability and bimetallic structure of the catalysts. Conversion of phenethyl phenyl ether continuously decreased with increasing Fe/Pd molar ratio, whereas selectivity for aromatics increased and then became almost constant with increasing Fe/Pd molar ratio. As a consequence, yield for aromatics showed a volcano-shaped trend with respect to Fe/Pd molar ratio. Catalytic performance of Pd_1–Fe_X/OMC catalysts was closely related to the hydrogen adsorption ability and bimetallic structure of the catalysts. Among the catalysts tested, Pd_1–$Fe_{0.7}$/OMC catalyst with moderate hydrogen adsorption ability and with bimetallic structure of $Pd_1Fe_{0.7}$ composition showed the highest yield for aromatics. Thus, an optimal Fe/Pd molar ratio was required to achieve maximum production of aromatics through selective cleavage of C—O bond in phenethyl phenyl ether over Pd_1–Fe_X/OMC catalysts.

1. Introduction

With increasing concerns about environmental problems and depletion of fossil fuels, lignocellulosic biomass has gained much attention as an alternative energy resource, because biofuels derived from biomass can reduce the dependence on fossil fuels and the emission of greenhouse gases [1–4]. However, it has been reported that only 2% of lignin by-products from pulp industries is used for commercial products such as binders in asphalt, cement or polymer [5–7]. Nevertheless, lignin is regarded as a promising source for sustainable production of fuels and platform chemicals, because lignin is an amorphous polymer produced by polymerization of coumaryl alcohol, coniferyl alcohol, and sinapyl alcohol [7,8]. Aromatic compounds in lignin are mainly linked by C—O and CC bonds such as β-*O*-4, α-*O*-4, 4-*O*-5, β-1, *β*–*β*, and 5-5 bonds. The amount of C—O bonds in lignin such as β-*O*-4 (40–60%), α-*O*-4 (3–5%), and 4-*O*-5 (4–7%) is much larger than the amount of CC bonds in lignin such as β-1 (7–9%), *β*–*β* (2–4%), and 5-5 (19–22%) [7,8]. Therefore, selective cleavage of C—O bond in lignin has been considered as a key strategy for the decomposition of lignin to aromatics.

Many attempts have been made on the lignin transformation into useful chemicals such as pyrolysis and catalytic and/or enzymatic depolymerization [7–10]. Among these methods, catalysis has attracted much attention as a promising process for selective conversion of lignin into value-added chemicals, because the reaction pathways can be controlled by appropriate selection of catalysts [7,11–13]. Noble metal catalysts such as Pt, Pd, and Rh are known to be effective for decomposition of C—O bond in lignin under mild conditions. Unfortunately, however, most of these catalysts tend to hydrogenate aromatic ring in lignin [7,14,15]. In order to improve aromatic production by selective cleavage of C—O bond in lignin without aromatic ring-saturation, therefore, noble metal-based bimetallic catalysts have been investigated [16–18]. The bimetallic systems can change the structural and electronic properties of noble metal catalysts, which induces a desired reaction

* Corresponding author. Fax: +82 2 889 7415.
E-mail address: inksong@snu.ac.kr (I.K. Song).

http://dx.doi.org/10.1016/j.molcata.2015.09.023
1381-1169/

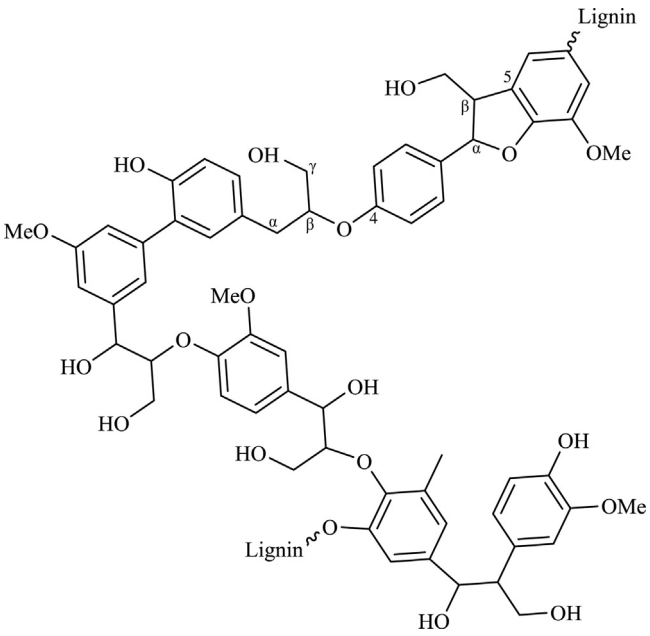

Fig. 1. Representative structure of a fragment of lignin.

pathway selectively [16–18]. For example, several bimetallic catalysts containing oxophilic metals such as Sn, Re, and Fe remarkably changed the product selectivity due to the improved interaction with the oxygenated group [19–22].

Fig. 1 shows the representative structure of a fragment of lignin. Due to the structural complexity of lignin, dimeric model compounds for representing C—O and CC bonds in lignin have been studied as a lignin feedstock for depoloymerization of lignin [7]. Lignin model compounds, which possess chemical linkages similar to lignin, can provide insight into the decomposition and reaction of lignin. In particular, dimeric lignin model compounds containing C—O bonds such as α-*O*-4, β-*O*-4, and β-5 bonds are generally used as lignin model compounds, because C—O bonds are abundant linkage type in lignin [7,8]. Among various lignin model compounds, phenethyl phenyl ether has been used as a lignin model compound for representing β-*O*-4 bond in lignin [7].

Porous carbon materials have been used for long time as a catalyst support [23,24]. In particular, ordered mesoporous carbon (OMC) can be potentially available as a supporting material because of uniform pore size distribution, efficient mass transfer of reactant molecules, and controllable textural properties [25–28]. In the selective cleavage of C—O bond in phenethyl phentyl ether, furthermore, carbon support can minimize the support effect due to its non-polar and hydrophobic nature [25,26]. These unique properties make OMC well suited as a potential candidate material for catalyst support.

In this work, a series of Pd–Fe bimetallic catalysts with different Fe/Pd molar ratio (*X*) were supported on ordered mesoporous carbon (Pd_1–Fe_X/OMC), and they were applied to the catalytic decomposition of phenethyl phenyl ether to aromatics. The effect of Fe/Pd molar ratio on the catalytic activities and physicochemical properties of the catalysts was investigated. The catalysts were characterized by nitrogen adsorption-desorption, TPR, XRD, STEM-EDX, TEM, H_2-TPD, and XPS analyses.

2. Experimental

2.1. Preparation of catalysts

A series of Pd–Fe bimetallic catalysts supported on ordered mesoporous carbon were prepared by a surfactant-templating method and a subsequent incipient wetness impregnation method. Ordered mesoporous carbon was prepared according to the method reported in the literature [28]. PEO-PPO-PEO tri-block copolymer (P123, Sigma–Aldrich) was dissolved in 1.5 M HCl solution

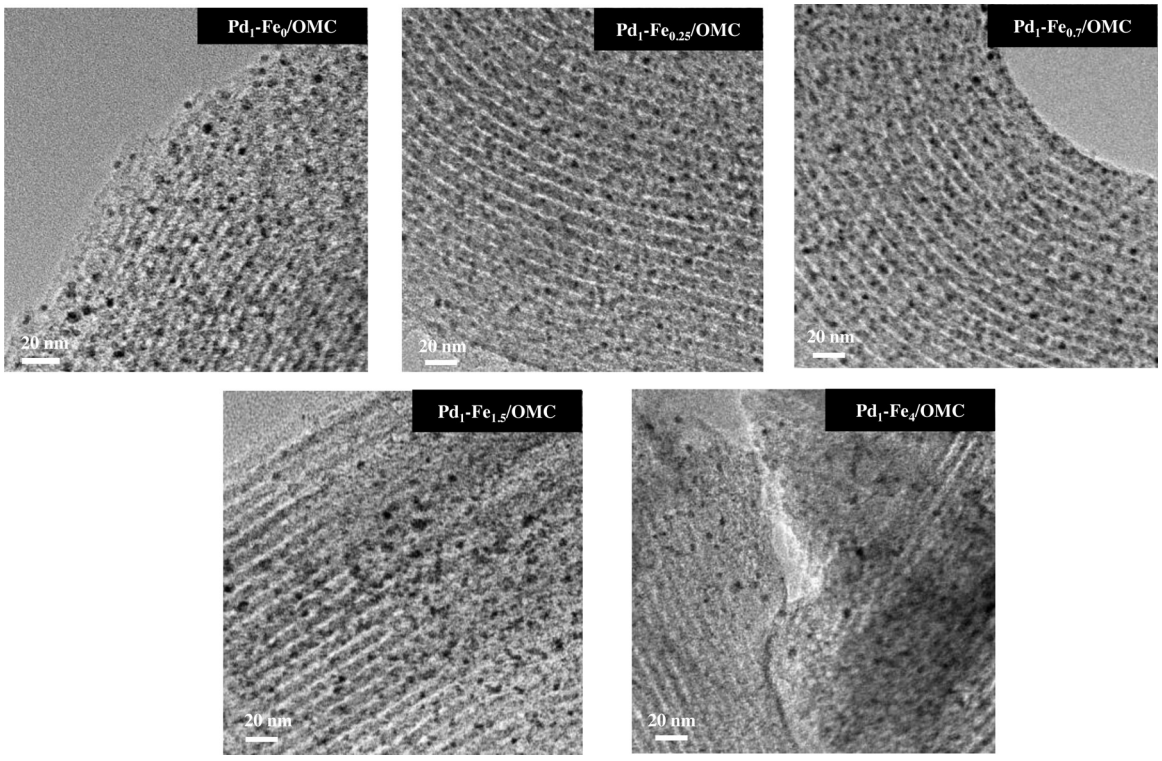

Fig. 2. HR-TEM images of reduced Pd_1–Fe_X/OMC (*X* = 0, 0.25, 0.7, 1.5, and 4) catalysts.

at 40 °C for 3 h. Sucrose (carbon precursor, TCI) and H_2SO_4 solution were then added into the solution for 1 h under stirring. After tetraethoxysilane (TEOS, Sigma–Aldrich) was slowly added into the solution, the resulting mixture was stirred at 40 °C for 24 h and then it was maintained at 100 °C for 20 h under static condition for self-assembly of micelle structure. The resultant was dried at 100 °C for 48 h, and it was carbonized at 800 °C for 4 h to obtain a silica-carbon composite. The silica-carbon composite was treated with 10 wt% HF solution to remove silica template, and it was finally filtered and dried. The resulting ordered mesoporous carbon was denoted as OMC.

For co-impregnation of palladium and iron metals onto OMC, palladium chloride ($PdCl_2$, Sigma–Aldrich) and iron nitrate ($Fe(NO_3)_3$, Junsei) were dissolved in acetone containing 0.1 M HCl. During this process, Pd:Fe molar ratio was adjusted to be 1:0, 0.8:0.2, 0.6:0.4, 0.4:0.6, and 0.2:0.8, while the total loading of two metals was fixed at 0.5 mol% in all samples to maintain the same number of active sites. The precursor solution was then introduced into the pores of OMC by an incipient wetness impregnation method. After drying the impregnated catalyst at 50 °C overnight, it was calcined at 450 °C for 3 h in a nitrogen stream. The supported catalyst was then reduced with a mixed stream of hydrogen (2.5 mL/min) and nitrogen (47.5 mL/min) at 450 °C for 4 h prior to the catalytic reaction. The prepared catalysts were denoted as Pd_1–Fe_X/OMC (X = 0, 0.25, 0.7, 1.5, and 4), where X represented the Fe/Pd molar ratio.

2.2. Characterization

For HR-TEM, nitrogen adsorption-desorption, ICP-AES, and XRD analyses of the reduced Pd_1–Fe_X/OMC (X = 0, 0.25, 0.7, 1.5, and 4) catalysts, ex-situ reduction of the catalysts was carried out under 5% H_2/Ar flow (50 mL/min) at 450 °C for 4 h. Pore structure and pore size of the reduced catalysts were examined by HR-TEM (JEM-3100, JEOL) analyses. In order to see the distribution of palladium and iron in the reduced catalysts, scanning transmission electron microscopy (STEM) analyses (JEM-2100F, JEOL) were conducted with energy dispersive X-ray spectroscopy (EDX) mapping.

Nitrogen adsorption–desorption measurements were conducted to investigate textural properties of the reduced catalysts using an ASAP-2010 (Micromeritics) instrument. Surface area of the reduced catalysts was measured by Brunaur–Emmett–Teller (BET) method [29]. Pore volume and average pore diameter were determined by the Barrett–Joyner–Halenda (BJH) method applied to the desorption branch of the N_2 isotherm [30].

Chemical compositions of the reduced catalysts were determined by ICP-AES analyses (Optima-4300 DV, Perkin-Elmer). Crystalline states of the reduced catalysts were examined by XRD (D-MAX-2500-PC, Rigaku) measurements using Cu–Kα radiation operated at 40 kV and 100 mA.

Temperature-programmed reduction (TPR) analyses of the calcined catalysts were conducted in a flow reactor system equipped with a thermal conductivity detector (TCD). 10 mg of each catalyst was reduced with a mixed stream of 5% H_2 (2 mL/min) and N_2 flow (20 mL/min) at temperatures ranging from room temperature to 500 °C with a heating rate of 10 °C/min.

H_2 temperature-programmed desorption (H_2-TPD) analyses of the reduced catalysts were conducted using a BELCAT-B instrument (BEL Japan). 10 mg of each calcined catalyst was preliminarily reduced at 450 °C for 4 h under 5% H_2/Ar flow (50 mL/min), and then it was purged with Ar flow (50 mL/min) for 10 min. After cooling the reduced catalyst to room temperature under Ar flow (50 mL/min), 5% H_2/Ar mixed gas (50 mL/min) was injected for 60 min at 250 °C. The sample was purged under Ar flow (50 mL/min) to remove physisorbed hydrogen, and subsequently, furnace temperature was increased from room temperature to 700 °C at a heating rate of 5 °C/min under Ar flow (50 mL/min). The desorbed hydrogen was detected using a TCD (thermal conductivity detector).

X-ray photoelectron spectroscopy (XPS) analyses (ThermoVG, Sigma probe) were carried out to measure binding energies of metallic palladium and iron in the reduced catalysts. For the XPS analyses, each calcined catalyst was reduced using an ex-situ reduction system at 450 °C for 4 h under 5% H_2/Ar flow (50 mL/min), and the catalyst was then transported to glass jar with sample holder in argon atmosphere glove box to minimize air exposure. After outgassing the glass jar in a vacuum oven, the sample holder was transferred to the XPS chamber as quickly as possible. All the XPS spectra were calibrated using C 1s peak (284.5 eV) as a reference.

2.3. Catalytic decomposition of phenethyl phenyl ether

Catalytic decomposition of phenethyl phenyl ether (PPE) to aromatics was carried out in a stainless steel autoclave reactor (25 mL) under hydrogen atmosphere. Prior to the reaction, each catalyst was reduced using an ex-situ reduction system at 450 °C for 4 h under 5% H_2/N_2 flow (50 mL/min). 50 mg of reduced catalyst, 0.25 g of phenethyl phenyl ether (Frinton Laboratory, a reactant), and 9 mL of hexadecane (Sigma–Aldrich, a solvent) were charged into the reactor at room temperature. The reactor was purged with nitrogen several times in order to remove air. The catalytic reaction was performed at 250 °C and 10 bar (H_2) for 3 h with agitation speed of 250 rpm. After the reaction, reaction products were analyzed using a gas chromatograph (Younglin, YL6100) equipped with a DB-1 column and a flame ionization detector (FID). Conversion of phenethyl phenyl ether and selectivity for aromatic product (benzene, phenol, or ethylbenzene) were calculated according to the following equations on the basis of mole balance. Yield for aromatic product (benzene, phenol, or ethylbenzene) was calculated by multiplying conversion of phenethyl phenyl ether and corresponding product selectivity.

$$\text{Conversion of phenethyl phenyl ether}\,(\%) = \frac{\text{moles of phenethyl phenyl ether reacted}}{\text{moles of phenethyl phenyl ether supplied}} \times 100 \quad (1)$$

$$\text{Selectivityforaromaticproduct\%} = \frac{\text{molesofbenzene,phenol,orethylbenzeneformed}}{\text{molesofphenethylphenyletherreacted}} \times 100 \quad (2)$$

$$\text{Yield for aromatic product}\,(\%) = \frac{(\text{Conversion of phenethyl phenyl ether}) \times (\text{Selectivity for aromatic})}{100} \quad (3)$$

3. Results and discussion

3.1. Characterization of catalysts

Fig. 2 shows the HR-TEM images of the reduced Pd_1–Fe_X/OMC (X = 0, 0.25, 0.7, 1.5, and 4) catalysts. All the catalysts had an ordered mesoporous carbon structure with pores in the range of 4–6 nm, and they retained well-dispersed metal particles. Small metal particles with an average size of ca. 4 nm were observed in the TEM images of the catalysts, indicating that metal species were uniformly dispersed in the channels or on the walls of OMC. There was no noticeable difference in metal particle size of Pd_1–Fe_X/OMC (X = 0, 0.25, 0.7, 1.5, and 4) catalysts.

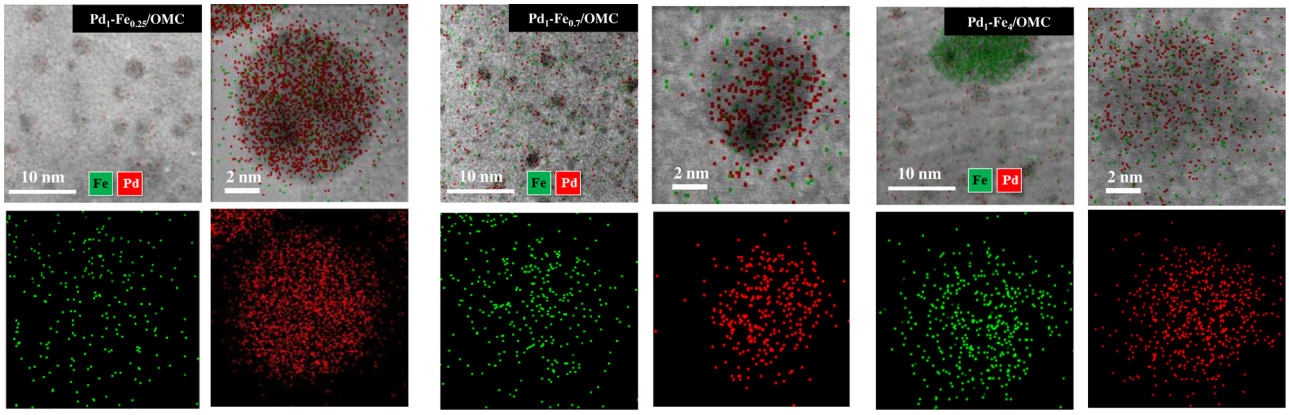

Fig. 3. STEM and EDX mapping images of Pd_1–Fe_X/OMC (X = 0.25, 0.7, and 4) catalysts.

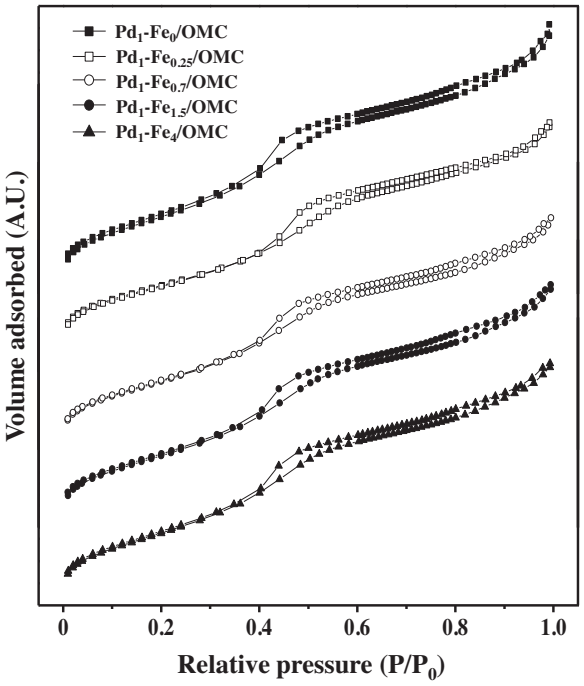

Fig. 4. Nitrogen adsorption–desorption isotherms of reduced Pd_1–Fe_X/OMC (X = 0, 0.25, 0.7, 1.5, and 4) catalysts.

In order to see the distribution of palladium and iron species, STEM-EDX analyses were conducted. Fig. 3 shows the STEM and EDX mapping images of Pd_1–Fe_X/OMC (X = 0.25, 0.7, and 4) catalysts. It is noteworthy that particles of palladium and iron species were homogeneously distributed in the bimetallic Pd–Fe_X/OMC catalysts. Moreover, population density of Fe increased with increasing Fe/Pd molar ratio. On the other hand, aggregation of Fe was observed when a large amount of Fe was added in the Pd–Fe_X/OMC catalyst (Pd_1–Fe_4/OMC). Therefore, it is inferred that a Pd–Fe miscible phase was partially formed in the bimetallic catalysts; the rest of iron was presented as metallic iron.

Fig. 4 shows the nitrogen adsorption-desorption isotherms of the reduced Pd_1–Fe_X/OMC (X = 0, 0.25, 0.7, 1.5, and 4) catalysts. All the catalysts exhibited type-IV isotherms with well-defined type-H3 hysteresis loops, indicating the formation of well-developed mesoporous structure [31,32]. Detailed textural properties of the reduced catalysts are summarized in Table 1. All the catalysts retained high surface area (>732 m^2/g), large pore volume (>0.88 cm^3/g), and large average pore diameter (> 4.0 nm). Surface area and pore volume of the catalysts slightly increased with increasing Fe/Pd molar ratio. This trend can be understood by the fact that the atomic radius of palladium (145 pm) is larger than that of iron (126 pm), which means that pore blockage by palladium is more severe than that by iron. However, average pore diameter of the catalysts was almost identical, suggesting that all the catalysts still retained pore characteristics of OMC. Chemical compositions of the reduced catalysts determined by ICP-AES analyses are also listed in Table 1. Actual Pd:Fe molar ratios of the catalysts were in good agreement with the designed values.

Crystalline phases of the reduced catalysts were examined by XRD measurements as shown in Fig. 5. All the catalysts showed a characteristic diffraction peak for graphitic carbon at $2\theta = 23.5^\circ$ [33]. The reduced Pd_1- Fe_0/OMC catalyst showed diffraction peaks at 40.1°, 46.6°, and 68.3°, corresponding to metallic palladium (closed circle in Fig. 5(a)) [34,35]. Fig. 5(b) shows the enlarged Pd (1 1 1) XRD patterns of Pd_1–Fe_X/OMC (X = 0, 0.25, 0.7, 1.5, and 4) catalysts. It was found that the characteristic diffraction peaks for palladium slightly but consistently shifted to higher angle in the Pd_1–Fe_X/OMC (X = 0, 0.25, 0.7, 1.5, and 4) catalysts with increasing Fe/Pd molar ratio. The Pd (1 1 1) peaks for Pd_1–Fe_X/OMC (X = 0, 0.25, 0.7, 1.5, and 4) catalysts appeared at 40.1°, 40.2°, 40.4°, 40.6°, and 40.7°, respectively (Fig. 5(b)). This consistent shift is an evidence for the formation of miscible phase between Pd and Fe through incorporation Fe atom into the lattice of Pd, as reported in the literatures [34,35]. On the other hand, diffraction peaks for metallic iron was not observed in the Pd_1–Fe_X/OMC (X = 0.25 and 0.7) catalysts due to its small crystalline size or low concentration (opened circle in Fig. 5(a) and (b)) [36,37]. However, Pd_1–Fe_X/OMC (X = 1.5 and 4) catalysts exhibited a diffraction peak for metallic iron (opened circle in Fig. 5(a) and (b)), and the peak intensity increased with increasing iron content. This is because both Pd_1–$Fe_{1.5}$/OMC and Pd_1–Fe_4/OMC catalysts had Fe enriched-surface by segregating Fe on the Pd–Fe surface, especially for the catalyst with higher Fe content (Fe/Pd ≥ 1.5) [18,38]. From XRD results, it was revealed that bimetallic phase of Pd_1–Fe_X/OMC catalysts were greatly affected by the Fe/Pd molar ratio.

It is known that H_2-TPR measurement is a powerful tool for examining reduction behavior and interaction between two metal species of the catalyst. Fig. 6 shows the TPR profiles of the calcined Pd_1–Fe_X/OMC (X = 0, 0.25, 0.7, 1.5, and 4) catalysts. TPR profile of Pd_1–Fe_0/OMC catalyst showed a negative peak at 60 °C and a positive peak at 170 °C; the former was attributed to the decomposition of palladium hydride phase (PdH_X) [39,40], while the latter was attributed to the reduction of palladium species [39,40]. Interestingly, the reduction behaviors of Pd_1–Fe_X/OMC (X = 0.25, 0.7, 1.5, and 4) catalysts were quite different depending on Fe/Pd molar ratio. For precise investigation, TPR profiles of Pd_1–Fe_X/OMC (X = 0.25, 0.7, 1.5, and 4) catalysts were decon-

Table 1
Textural properties of reduced Pd_1–Fe_X/OMC (X = 0, 0.25, 0.7, 1.5, and 4) catalysts.

Catalyst	Pd: Fe molar ratio[a]	Surface area (m^2/g)[b]	Pore volume (cm^3/g)[c]	Pore diameter (nm)[d]
Pd_1–Fe_0/OMC	–	732	0.88	4.1
Pd_1–$Fe_{0.25}$/OMC	0.21: 0.79	750	0.90	4.2
Pd_1–$Fe_{0.7}$/OMC	0.40: 0.60	762	0.91	4.0
Pd_1–$Fe_{1.5}$/OMC	0.61: 0.39	772	0.92	4.1
Pd_1–Fe_4/OMC	0.81: 0.19	782	0.94	4.3

[a] Determined by ICP-AES measurement.
[b] Calculated by the BET equation.
[c] Total pore volume at P/P_0 = 0.99.
[d] Average pore diameter.

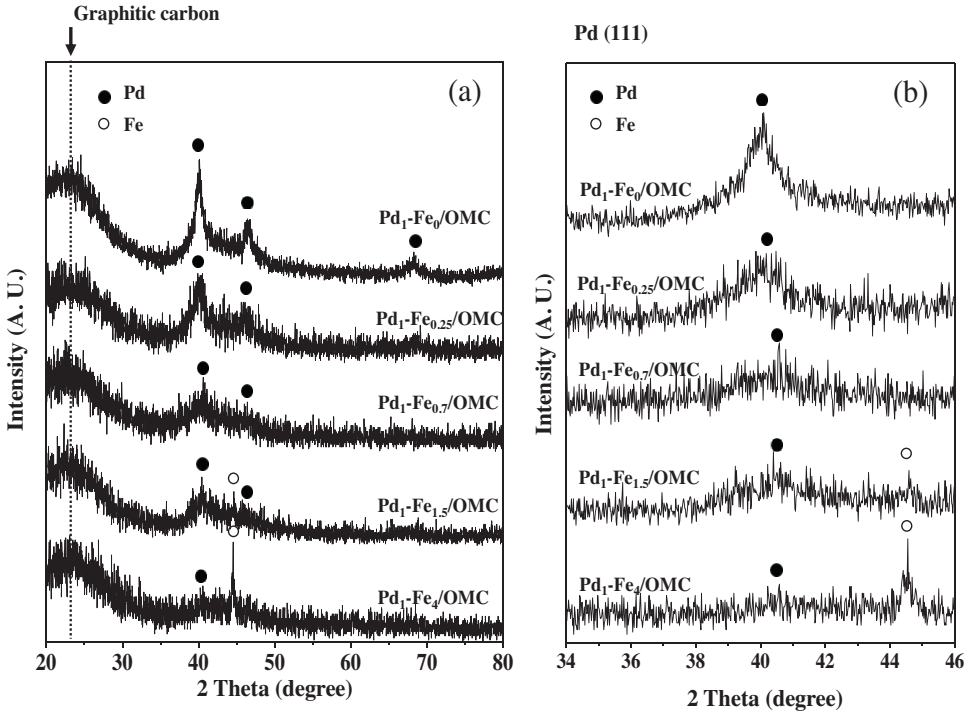

Fig. 5. XRD patterns of (a) reduced Pd_1–Fe_X/OMC catalysts and (b) enlarged Pd (1 1 1) diffraction peaks for Pd_1–Fe_X/OMC catalysts.

voluted. As shown in Fig. 6, bimetallic Pd_1–Fe_X/OMC (X = 0.25, 0.7, 1.5, and 4) catalysts showed three deconvoluted reduction peaks. In our previous work [38], it was reported that the reduction of Fe catalyst supported on ordered mesoporous carbon (Fe/OMC) occurred through three steps. Fe_2O_3 was reduced to Fe_3O_4 (335 °C) in the first step. The second step involved the reduction of Fe_3O_4 to FeO (496 °C), which was subsequently reduced to metallic Fe (596 °C). As shown in Fig. 6, Pd_1–Fe_X/OMC (X = 0.25, 0.7, 1.5, and 4) catalysts also showed three distinct peaks, but the peaks moved toward low temperature compared to those of Fe/OMC catalyst. It is well known that reducibility of bimetallic catalyst was strongly affected by the interaction between two metal species [40,41]. In particular, bimetallic catalysts containing noble metal facilitate the reduction of other transition metal due to hydrogen transfer from their reduced species [41,42]. Therefore, it can be inferred that activated hydrogen on the reduced palladium species was transferred to unreduced Fe species during the reduction process, which promoted the reduction of Fe species. In addition, the negative peak corresponding to palladium hydride (PdH_X) disappeared upon addition of Fe, indicating that iron species suppressed the formation of PdH_X phases due to the strong interaction between metal species [39]. With increasing Fe content (Fe/Pd ≥ 1.5), furthermore, intensity of reduction peak above 350 °C was remarkably increased. This might be because a fraction of Fe remained as metallic species on the carbon support, as evidenced by XRD results. Thus, it is expected that Pd and Fe fractions were co-reduced by partially forming a Pd–Fe bimetallic phase. From XRD and TPR results, it can be inferred that bimetallic phase could be controlled by changing Fe/Pd ratio, which might strongly affect the catalytic performance.

3.2. Catalytic performance in the decomposition of phenethyl phenyl ether

Fig. 7 shows the reaction pathways for decomposition of phenethyl phenyl ether (PPE). According to the literatures [43,44], the cleavage of β-*O*-4 linkage follows parallel-consecutive reaction pathways. Aromatic compounds are produced by the cleavage of Cβ—O bond in phenethyl phenyl ether, and consecutive hydrogenation of aromatic ring leads to the formation of aromatic ring-saturated products. On the other hand, hydrogenation of aromatic ring in phenethyl phenyl ether occurs prior to Cβ—O bond cleavage, which also produces aromatic ring-saturated products. In our catalytic reaction, aromatic compounds such as benzene, phenol, and ethylbenzene were produced by the cleavage of C—O bond in phenenthyl phenyl ether. Aromatic ring-saturated products including cyclohexane derivatives (cyclohexane, cyclohexanol, and ethylcyclohexane) and fully hydrogenated PPE were also produced by the hydrogenation of aromatic rings. Light hydrocarbon (C_1–C_3) and phenylethyl benzene were produced as by- products.

Table 2
Catalytic performance of reduced Pd_1–Fe_X/OMC (X = 0, 0.25, 0.7, 1.5, and 4) catalysts in the catalytic decomposition of phenethyl phenyl ether (PPE) performed at 250 °C and 10 bar for 3 h.

Catalyst	Conversion of PPE (%)	Selectivity (%)							Yield for aromatics
		Aromatics			Total selectivity for aromatics	Aromatic ring-saturated product		By-products	
		Benzene	Phenol	Ethylbenzene		Cyclohexane derivatives	Fully hydrogenated PPE		
No catalyst	3.2	2.7	40.3	34.5	77.5	2.8	2.5	17.2	2.5
Pd_1–Fe_0/OMC	94.1	7.2	5.4	3.4	16.0	59.3	15.6	9.1	15.1
Pd_1–$Fe_{0.25}$/OMC	88.3	13.6	6.2	12.3	32.1	48.5	9.8	9.6	28.3
Pd_1–$Fe_{0.7}$/OMC	75.6	26.5	21.3	27.2	75.0	12.4	2.6	10.0	56.7
Pd_1–$Fe_{1.5}$/OMC	63.2	22.8	23.3	27.6	73.7	10.8	6.1	9.4	46.6
Pd_1–Fe_4/OMC	41.2	21.4	25.6	28.4	75.4	8.5	6.2	9.9	31.1

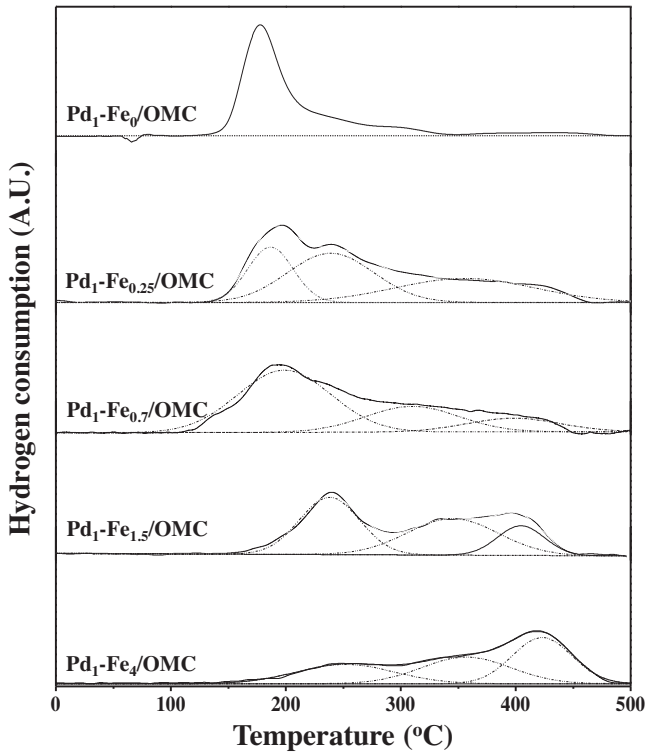

Fig. 6. TPR profiles of calcined Pd_1–Fe_X/OMC (X = 0, 0.25, 0.7, 1.5, and 4) catalysts.

Catalytic performance of the reduced Pd_1–Fe_X/OMC (X = 0, 0.25, 0.7, 1.5, and 4) catalysts in the decomposition of phenethyl phenyl ether performed at 250 °C and 10 bar for 3 h is summarized in Table 2. In the absence of catalyst, conversion of phenethyl phenyl ether was very low although selectivity for aromatics was high, resulting in low yield for aromatics. This result indicates that catalytic decomposition of phenethyl phenyl ether does not proceed in the absence of catalyst because C—O and CC bonds are thermally stable. All the catalysts showed an enhanced conversion of phenethyl phenyl ether compared to the case of no catalyst. Pd_1–Fe_0/OMC catalyst was very active for hydrogenation of aromatic ring in phenethyl phenyl ether, leading to the formation of aromatic ring-saturated products. On the other hand, bimetallic catalysts showed the relatively low activity toward hydrogenation of aromatic ring. Catalytic performance of Pd_1–Fe_X/OMC (X = 0, 0.25, 0.7, 1.5, and 4) catalysts was strongly influenced by Fe/Pd molar ratio. In order to visualize the effect of Fe/Pd molar ratio on the catalytic performance of bimetallic Pd_1–Fe_X/OMC (X = 0, 0.25, 0.7, 1.5, and 4) catalysts, conversion of phenethyl phenyl ether, selectivity for aromatics, and yield for aromatics were plotted as a function of Fe/Pd molar ratio (X) as shown in Fig. 8. Conversion of phenethyl phenyl ether decreased with increasing Fe/Pd molar ratio. On the other hand, selectivity for aromatics increased with increasing Fe/Pd molar ratio up to 0.7 (Fe/Pd < 0.7), but it was almost constant at high Fe/Pd molar ratio (Fe/Pd ≥ 0.7). The compensation between conversion of phenethyl phenyl ether and selectivity for aromatics led to a volcano-shaped curve of aromatic yield with respect to Fe/Pd molar ratio. Thus, an optimal Fe/Pd molar ratio was required for achieving maximum catalytic performance toward aromatic production. Among the catalysts tested, Pd_1–$Fe_{0.7}$/OMC catalyst showed the highest yield for aromatics.

Table 3
H_2-TPD results of reduced Pd_1–Fe_X/OMC (X = 0, 0.25, 0.7, 1.5, and 4) catalysts.

Catalyst	Amount of desorbed hydrogen (μmol-H_2/g-cat.)[a]
Pd_1–Fe_0/OMC	128.2
Pd_1–$Fe_{0.25}$/OMC	92.9
Pd_1–$Fe_{0.7}$/OMC	79.1
Pd_1–$Fe_{1.5}$/OMC	52.8
Pd_1–Fe_4/OMC	37.8

[a] Calculated from peak area of H_2-TPD profile (<600 °C) in Fig. 7.

3.3. Hydrogen adsorption study on the reduced Pd_1–Fe_X/OMC catalysts

Catalytic decomposition of lignin through hydrogenation (including hydrogenolysis) on metal sites occurs via following steps; (1) gas phase hydrogen is dissociatively adsorbed and activated on the surface of metal sites, and (2) adsorbed hydrogen on the surface of metal sites reacts with oxygen groups of reactant or C=C bond in lignin, leading to the cleavage of C—O or C=C bond in reactant, respectively. Therefore, hydrogen adsorption ability on the surface of metal sites plays an important role in the catalytic decomposition of lignin model compounds [45,46]. For this reason, H_2-TPD measurement was carried out in order to investigate the hydrogen adsorption ability of the reduced catalysts.

Fig. 9 shows the H_2-TPD profiles of the reduced Pd_1–Fe_X/OMC (X = 0, 0.25, 0.7, 1.5, and 4) catalysts. H_2-TPD profiles of the reduced catalysts could be deconvoluted into two hydrogen desorption peaks. According to the literature [47], the peak above 600 °C is related to the gasification of carbon support. In this work, therefore, hydrogen desorption peak below 600 °C, which was related to the desorption of hydrogen from the reduced palladium and iron species, was only considered for quantification. The amount of desorbed hydrogen was calculated from the deconvoluted peak area of H_2-TPD profile (<600 °C), as listed in Table 3. It was found that the amount of desorbed hydrogen was greatly affected by Fe/Pd molar ratio. The amount of hydrogen desorbed from the reduced catalysts decreased in the order of Pd_1–Fe_0/OMC > Pd_1–$Fe_{0.25}$/OMC > Pd_1–$Fe_{0.7}$/OMC > Pd_1–$Fe_{1.5}$/

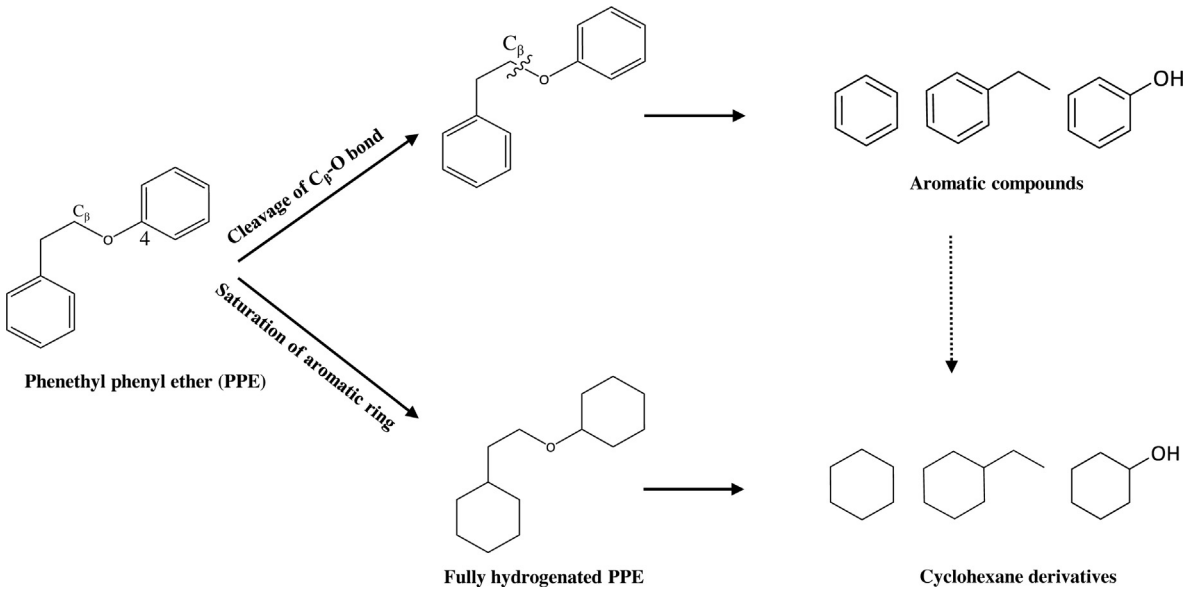

Fig. 7. Reaction pathways for decomposition of phenethyl phenyl ether (PPE).

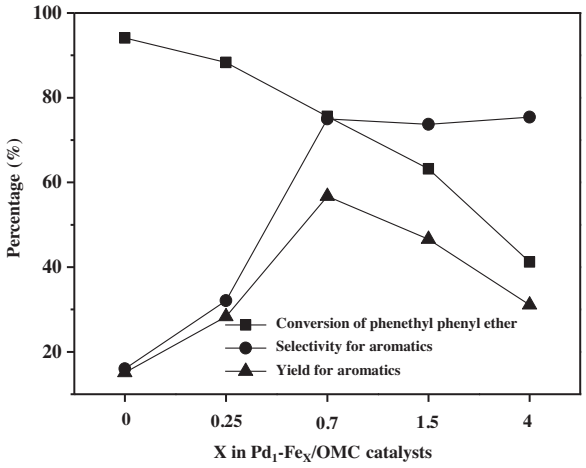

Fig. 8. Catalytic performance of Pd_1–Fe_X/OMC (X = 0, 0.25, 0.7, 1.5, and 4) catalysts in the decomposition of phenethyl phenyl ether, plotted as a function of Fe/Pd molar ratio (X). Reaction conditions: temperature = 250 °C, pressure = 10 bar (H_2), and time = 3 h.

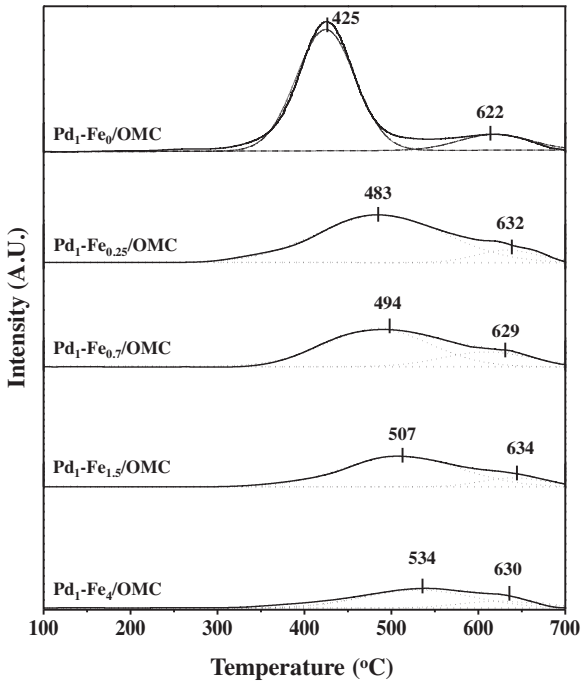

Fig. 9. H_2-TPD profiles of reduced Pd_1–Fe_X/OMC (X = 0, 0.25, 0.7, 1.5, and 4) catalysts.

OMC > Pd_1–Fe_4/OMC. This trend was well consistent with the trend of conversion of phenethyl phenyl ether (Fig. 8). It is known that the enhancement in the amount of chemisorbed hydrogen is beneficial to improve the catalytic activity. However, it was observed that Pd_1–Fe_0/OMC catalyst had a strong tendency to saturate aromatic ring in the reaction. This is because the surface of Pd with strong hydrogen adsorption ability stabilizes the π-bonded complex with aromatic rings and participates in hydrogenation, resulting in cleavage of C=C bond in aromatic ring [18]. With increasing Fe/Pd molar ratio, on the other hand, conversion of phenethyl phenyl ether was monotonically decreased (Fig. 8). This trend can be explained by the dilution effect of inactive Fe onto Pd, which decreases the total number of available active sites for hydrogen adsorption. Therefore, it is believed that moderate hydrogen adsorption ability was required for enhanced aromatic production. However, no correlation between hydrogen adsorption ability and aromatic selectivity was found. Therefore, our next investigation was focused on the effect chemical state of metal species on the aromatic selectivity. For this purpose, XPS analyses of the reduced Pd_1–Fe_X/OMC (X = 0, 0.25, 0.7, 1.5, and 4) catalysts were carried out.

3.4. XPS study of reduced Pd_1–Fe_X/OMC catalysts

Fig. 10 shows the XPS spectra of Pd 3d (Fig. 10(a)) and Fe $2p_{3/2}$ (Fig. 10(b)) levels of the reduced Pd_1–Fe_X/OMC (X = 0, 0.25, 0.7, 1.5, and 4) catalysts. The Pd 3d spectra were deconvoluted into $Pd_{5/2}$ (solid line) and $Pd_{3/2}$ (dashed line) peaks, and then Pd 3d spectra were divided into Pd^0 (335.2 eV and 340.5 eV for $3d_{5/2}$ and $3d_{3/2}$, respectively) and Pd^{2+} (337.1 eV and 341.9 eV for $3d_{5/2}$ and $3d_{3/2}$, respectively) species [48,49]. The Fe $2p_{3/2}$ spectra were assigned to metallic Fe^0 (707.6 eV), Fe^{2+} (709.6 eV), and Fe^{3+} (710.9 eV) species [50]. Interestingly, the binding energy of Pd 3d

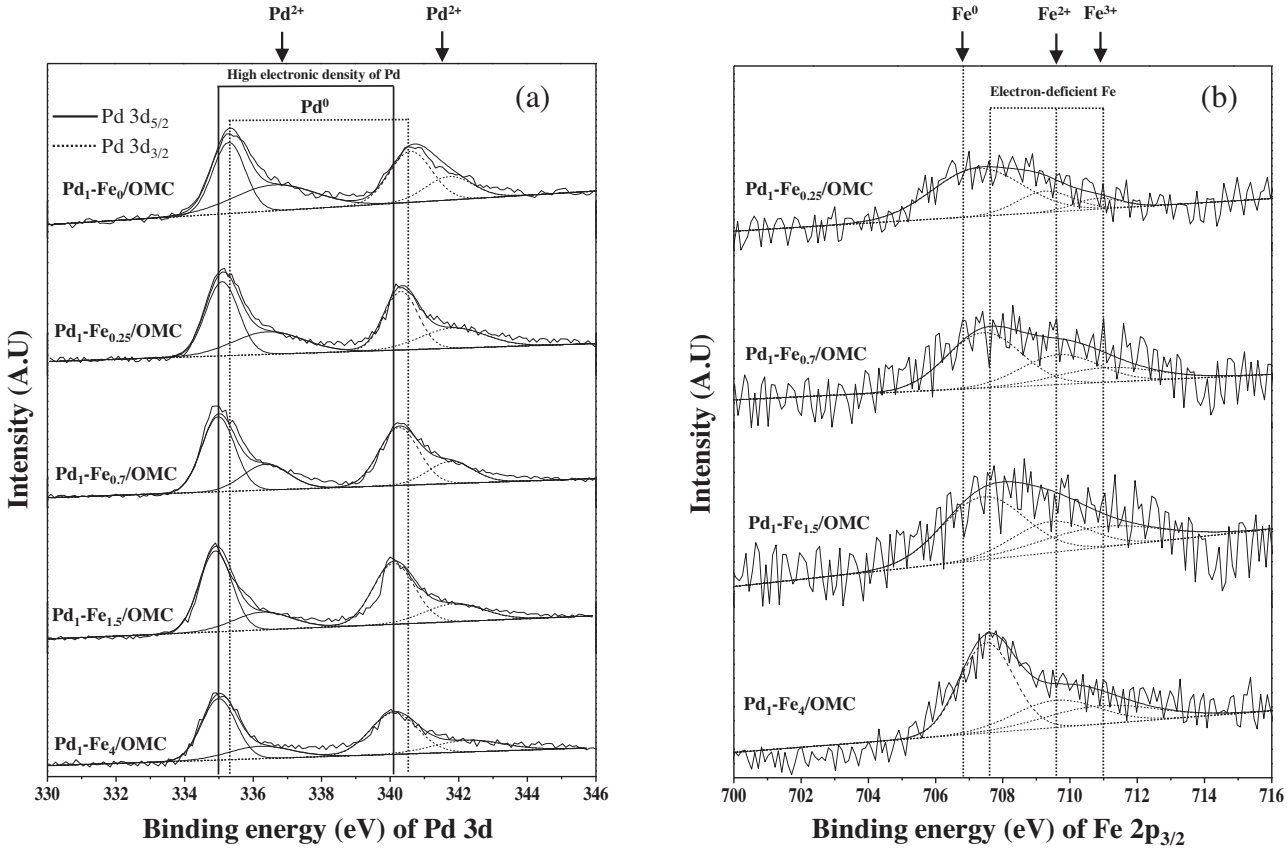

Fig. 10. XPS spectra of (a) Pd 3d and (b) Fe $2p_{3/2}$ levels in the reduced Pd_1–Fe_X/OMC (X = 0, 0.25, 0.7, 1.5, and 4) catalysts.

Table 4
XPS analyses results of reduced Pd_1–Fe_X/OMC (X = 0, 0.25, 0.7, 1.5, and 4) catalysts.

Catalyst	Ratio of Pd species[a]	Ratio of Fe species[a]	$Fe^{\delta+}/Pd$[b]	$Fe^{\delta+}/(Pd^0+Fe^{\delta+})$[b]	Composition of bimetallic structure
	Pd^0/Pd_{total}	$Fe^{\delta+}/Fe_{total}$[b]			
Pd_1–Fe_0/OMC	0.52	–	–	–	–
Pd_1–$Fe_{0.25}$/OMC	0.59	0.28	0.49	0.29	$Pd_1Fe_{0.4}$
Pd_1–$Fe_{0.7}$/OMC	0.68	0.45	0.65	0.40	$Pd_1Fe_{0.7}$
Pd_1–$Fe_{1.5}$/OMC	0.73	0.47	0.66	0.39	$Pd_1Fe_{0.7}$
Pd_1–Fe_4/OMC	0.74	0.49	0.65	0.40	$Pd_1Fe_{0.7}$

[a] Calculated from deconvoluted peak area of XPS spectra in Fig. 8.
[b] $2 \le \delta \le 3$.

level in the Pd_1–Fe_X/OMC (X = 0.25, 0.7, 1.5, and 4) catalysts slightly shifted toward low value with increasing Fe/Pd molar ratio (Fig. 10 (a)). On the other hand, the binding energy of Fe $2p_{3/2}$ level in the Pd_1–Fe_X/OMC (X = 0.25, 0.7, 1.5, and 4) catalysts shifted toward high value with increasing Fe/Pd molar ratio (Fig 10(b)). The change of electronic properties was attributed to charge transfer from Fe to Pd, which was related to the relative electronegativity of each metal (1.8 and 2.2 for Fe and Pd, respectively, according to the Pauling's scale) [34,35]. The charge transfer between two metal species induces polarity on bimetallic phase. In the case of Pd on the Pd–Fe surface, electron-rich palladium atoms decreased the stability of π-bonded complex with aromatic ring, resulting in the suppressed rate of hydrogenation of C=C bond in aromatics. In the case of Fe on the Pd–Fe surface, on the other hand, electron- deficient Fe atoms acted as adsorption sites for activating oxygenated group and facilitating hydrogenation of C—O bond in phenethyl phenyl ether. For this reason, bimetallic Pd_1–Fe_X/OMC (X = 0.25, 0.7, 1.5, and 4) catalysts were more efficient in the selective cleavage of C—O bond in phenethyl phenyl ether to aromatics than Pd_1–Fe_0/OMC catalyst. Judging from XPS results, it can be inferred that electron-deficient iron atoms ($Fe^{\delta+}$) was in contact with metallic palladium atoms (Pd^0), forming a bimetallic phase on the catalyst surface [51,52] . In order to confirm the chemical state of bimetallic phase in the Pd_1–Fe_X/OMC catalysts, the chemical state ratios of Pd and Fe were quantified as summarized in Table 4. Chemical state of each metal species was obtained by integrating each deconvoluted XPS peak area for Pd and Fe species. It was found that Pd^0/Pd_{total} increased with increasing Fe/Pd molar ratio, and $Fe^{\delta+}/Fe_{total}$ also increased with increasing Fe/Pd molar ratio. Interestingly, $Fe^{\delta+}/Pd$ showed no significant difference at high Fe/Pd molar ratio above 0.7. This result suggests that Pd and Fe are in contact with each other in the same molar ratio at high Fe/Pd molar ratio above 0.7. In addition, the result of $Fe^{\delta+}/(Pd^0+Fe^{\delta+})$ molar ratios of Pd_1–Fe_X/OMC (X = 0.7, 1.5, and 4) catalysts revealed that the bimetallic catalysts were mainly composed of bimetallic structure of $Pd_1Fe_{0.7}$ composition at high Fe/Pd molar ratio above 0.7; the remaining fraction of metal species existed as a metallic state on the carbon support, as evidenced by STEM-EDX, XRD and TPR results. This result was well consistent with the previous work [34], reporting that metallic Fe alone

was catalytically inactive for the hydrogenation C=C bond in aromatics. Thus, it is inferred that the bimetallic structure of $Pd_1Fe_{0.7}$ composition of the catalysts was mainly responsible for high and constant selectivity for aromatics at Fe/Pd $\geq$ 0.7 in the selective cleavage of C—O bond in phenethyl phenyl ether (Table 4 and Fig. 8). Another noticeable point is that binding energy of metallic Fe in the Pd_1–$Fe_{0.25}$/OMC was 707.2 eV. This binding energy value of metallic Fe in the Pd_1–$Fe_{0.25}$/OMC catalyst was slightly higher than $2p_{3/2}$ binding energy of metallic iron which was reported to be 706.8 eV [53]. Considering that the binding energy shift was closely related to the binding strength of two metals [54,55], it is expected that the interaction does not lead to the complete formation of bimetallic phase due to low concentration of Fe. Therefore, it is concluded that saturation of aromatics ring was not effectively suppressed over the bimetallic catalyst with low Fe content (Pd_1–$Fe_{0.25}$/OMC).

On the basis of H_2-TPD and XPS results, it is believed that an optimal Fe/Pd molar ratio was required for the formation of bimetallic structure of $Pd_1Fe_{0.7}$ composition and for the moderate hydrogen adsorption ability, and in turn, for the highest yield for aromatics over Pd_1–Fe_X/OMC (X = 0, 0.25, 0.7, 1.5, and 4) catalysts.

4. Conclusions

A series of bimetallic Pd-Fe catalysts supported on ordered mesoporous carbon (Pd_1–Fe_X/OMC, X = 0, 0.25, 0.7, 1.5, 4) were characterized and evaluated in order to find optimum Fe/Pd molar ratio for maximum production of aromatics through catalytic decomposition of phenethyl phenyl ether (a model compound for representing β-*O*-4 bond in lignin). It was found that physicochemical properties of bimetallic catalysts were greatly affected by Fe/Pd molar ratio. In particular, interaction between Pd and Fe resulted in the modification of electronic properties of Pd by electronic transfer from Fe to Pd, which remarkably changed the hydrogen adsorption ability and bimetallic structure. In the catalytic decomposition of phenethyl phenyl ether to aromatics, hydrogen adsorption ability and bimetallic structure of the catalysts were closely related to conversion of phenthyl phenyl ether and selectivity for aromatics, respectively. Conversion of phenthyl phenyl ether decreased with increasing hydrogen adsorption ability, while maximum selectivity for aromatics was obtained when the bimetallic structure of $Pd_1Fe_{0.7}$ was formed. Among the catalysts tested, Pd_1–$Fe_{0.7}$/OMC catalyst with moderate hydrogen adsorption ability and with bimetallic structure of $Pd_1Fe_{0.7}$ composition showed the best catalytic performance in terms of yield for aromatics.

Acknowledgements

This work was supported by the National Research Foundation of Korea Grant funded by the Korean Government (MEST) (NRF-2012M1A2A2671739).

References

[1] C.E. Wyman, Bioresour. Technol. 50 (1994) 3–15.
[2] M. Stöcker, Angew. Chem. Int. Ed. 47 (2008) 9200–9211.
[3] H.L. Chum, R.P. Overend, Fuel Process. Technol. 71 (2001) 187–195.
[4] A. Demirbaş, Energy Convers. Manage. 42 (2001) 1357–1378.
[5] D. Stewart, Ind. Corp Prod. 27 (2008) 202–207.
[6] R.J.A. Grosselink, E. de Jong, D. Guran, A. Aächerli, Ind. Crop Prod. 20 (2004) 121–129.
[7] J. Zakzeski, P.C.A. Bruijnincx, A.L. Jongerius, B.M. Weckhuysen, Chem. Rev. 110 (2010) 3552–3599.
[8] A.-C. Carlos, H. Pakdel, C. Roy, Bioresour. Technol. 79 (2001) 277–299.
[9] M.P. Pandey, C.S. Kim, Chem. Eng. Technol. 34 (2011) 29–41.
[10] C. Xu, R.A.D. Arancon, J. Labidi, R. Luque, Chem. Soc. Rev. 43 (2014) 7488–7500.
[11] A.P.S. Chouhan, A.K. Sarma, Renew. Sust. Energy Rev. 15 (2011) 4378–4399.
[12] M. Zabeti, W.M.A.W. Daud, M.K. Aroua, Fuel Process. Technol. 90 (2009) 770–777.
[13] M.A. Jackson, D.L. Compton, A.A. Boateng, J. Anal. Appl. Pyrol. 85 (2009) 226–230.
[14] N. Yan, C. Zhao, P.J. Dyson, C. Wang, L.-T. Liu, Y. Kou, ChemSusChem 1 (2008) 626–629.
[15] K. Yoon, A. Vannice, J. Catal. 82 (1983) 457–468.
[16] A.K. Singh, Q. Xu, ChemCatChem 5 (2013) 652–676.
[17] J. Zhang, J. Teo, X. Chen, H. Asakura, T. Tenaka, K. Teramura, N. Yan, ACS Catal. 4 (2014) 1574–1583.
[18] J. Sun, A.M. Karim, H. Zhang, L. Kovarik, X.S. Li, A.J. Hensley, J.-S. McEwen, Y. Wang, J. Catal. 306 (2013) 47–57.
[19] L.L.P.M. De Souza, F.B. Noronha, W. An, T. Sooknoi, D.E. Resasco, J. Mol. Catal. A: Chem. 388–389 (2014) 47–55.
[20] J.P. Stassi, P.D. Zgolicz, S.R. De Miguel, O.A. Scelza, J. Catal. 306 (2013) 11–29.
[21] L. Ma, D. He, Top Catal. 52 (2009) 834–844.
[22] J. Zhang, H. Asakura, J.V. Rijn, J. Yang, P. Duchesne, B. Zhang, P. Zhang, M. Saeys, N. Yang, Green Chem. 16 (2014) 2432–2437.
[23] Q. Wang, H. Li, L. Chen, X. Huang, Carbon 39 (2001) 2211–2214.
[24] J.L. Zimmerman, R. Williams, V.N. Khabashesku, J.L. Margrave, Nano Lett. 1 (2001) 731–734.
[25] M. Kruk, M. Jaroniec, T.W. Kim, R. Ryoo, Chem. Mater. 15 (2003) 2815–2823.
[26] E.J. Zanto, S.A. Al- Muhtaseb, J.A. Ritter, Ind. Eng. Chem. Res. 41 (2002) 3151–3162.
[27] S. Che, S. Kamiya, O. Terasaki, T. Tatsumi, J. Am. Chem. Soc. 123 (2001) 12089–12090.
[28] C.C. Ting, H.Y. Wu, S. Vetrivel, D. Saikia, Y.C. Pan, G.T.K. Fey, H.M. Kao, Microporous Mesoporous Mater. 128 (2010) 1–11.
[29] S. Brunauer, P.H. Emmett, E. Teller, J. Am. Chem. Soc. 60 (1938) 309–319.
[30] E.P. Barrett, L.G. Joyner, P.P. Halenda, J. Am. Chem. Soc. 73 (1951) 373–380.
[31] M. Kruk, M. Jaroniec, Y. Bereznitski, J. Colloid Interface Sci. 182 (1996) 282–288.
[32] I. Matos, S. Fernandes, L. Guerreiro, S. Barata, A.M. Ramos, J. Vital, I.M. Fonseca, Microporous Mesoporous Mater. 92 (2006) 38–46.
[33] Z.Q. Li, C.J. Lu, Z.P. Xia, Y. Zhou, Z. Luo, Carbon 45 (2007) 1686–1695.
[34] M. Liao, Q. Hu, J. Zheng, Y. Li, H. Zhou, C.-J. Zhong, B.H. Chen, Electrochim. Acta 111 (2013) 504–509.
[35] W. Wang, D. Zheng, C. Du, Z. Zou, X. Zhang, B. Xia, H. Yang, D.L. Akins, J. Power Sourc. 167 (2007) 243–249.
[36] D. Sun, G. Zhang, X. Jiang, J. Huang, X. Jing, Y. Zheng, J. He, Q. Li, J. Mater. Chem. A 2 (2014), 1767–1733.
[37] J. Li, J. Gu, H. Li, Y. Liang, Y. Hao, X. Sun, L. Wang, Microporous Mesoporous Mater. 128 (2010) 144–149.
[38] J.K. Kim, J.K. Lee, K.H. Kang, J.C. Song, I.K. Song, Appl. Catal. A 498 (2015) 142–149.
[39] F. Pinna, M. Selva, M. Signoretto, G. Strukul, F. Boccuzzi, A. Benedetti, P. Canton, G. Fagherazzi, J. Catal. 150 (1994) 356–367.
[40] A. Benedetti, G. Fagherazzi, F. Pinna, G. Rampazzo, M. Selva, G. Strukul, Catal. Lett. 10 (1991) 215–224.
[41] Y. Hong, H. Zhang, J. Sun, K.M. Ayman, A.J.R. Hensley, M. Gu, M.H. Engelhard, J.-S. McEwen, Y. Wang, ACS Catal. 4 (2014) 3335–3345.
[42] O.E. Lebedeva, W.M.H. Sachtler, J. Catal. 191 (2000) 364–372.
[43] Q. Song, J. Cai, J. Zhang, W. Yu, F. Wang, J. Xu, Chin. J. Catal. 34 (2013) 651–658.
[44] M.W. Jarvis, J.W. Daily, H.-H. Carstensen, A.M. Dean, S. Sharma, D.C. Dayton, D.J. Robichaud, M.R. Nimlos, J. Phys. Chem. A 115 (2011) 428–438.
[45] H.Y. Zhao, D. Li, P. Bui, S.T. Oyama, Appl. Catal. A 391 (2011) 305–310.
[46] M. Nagai, Appl. Catal. A 322 (2007) 178–190.
[47] X. Dong, H.-B. Zhang, G.-D. Lin, Y.-Z. Yuan, K.R. Yasi, Catal. Lett. 85 (2003) 237–246.
[48] Y. Tang, S. Cao, Y. Chen, T. Lu, Y. Zhou, L. Lu, J. Bao, Appl. Surf. Sci. 256 (2010) 4196–4200.
[49] Y. Pan, F. Zhang, K. Wu, Z. Lu, Y. Chen, Y. Zhou, Y. Tang, T. Lu, Int. J. Hydrogen Energy 37 (2012) 2993–3000.
[50] J. Leveneur, G.I.N. Waterhouse, J. Kennedy, J.B. Metson, D.R.G. Mitchel, J. Phys. Chem. C 115 (2011) 20978–20985.
[51] D. Richard, J. Ockelford, A. Giroir- Fendler, P. Gallezot, Catal. Lett. 3 (1989) 53–58.
[52] M.A. Aramendía, V. Borau, C. Jiménez, J.M. Marinas, A. Porras, F.J. Ubrano, J. Catal. 172 (1997) 46–54.
[53] P.C.J. Graat, M.A.J. Somers, Appl. Surf. Sci. 100–101 (1996) 36–40.
[54] Z. Lui, X. Tan, J. Li, C. Lv, New J. Chem. 37 (2013) 1350–1357.
[55] J.A. Rodriguez, D.W. Goodman, Science 257 (1992) 897–903.